Hetero-interpenetrated metal-organic frameworks

David Perl
Massey University https://orcid.org/0000-0003-2757-0292
Seok Lee
Massey University https://orcid.org/0000-0002-8061-6002
Alan Ferguson
Massey University
Geoffrey Jameson
Massey University https://orcid.org/0000-0003-4839-0784
Shane Telfer (S.Telfer@massey.ac.nz)
Massey University https://orcid.org/0000-0003-1596-6652

Article

Keywords:

Posted Date: February 17th, 2022

DOI: https://doi.org/10.21203/rs.3.rs-1342292/v1

Hetero-interpenetrated metal-organic frameworks

David Perl, Seok J. Lee, Alan Ferguson, Geoffrey B. Jameson and Shane G. Telfer*

MacDiarmid Institute for Advanced Materials and Nanotechnology; School of Natural Sciences, Massey University, Palmerston North, New Zealand.

Email: s.telfer@massey.ac.nz

Abstract

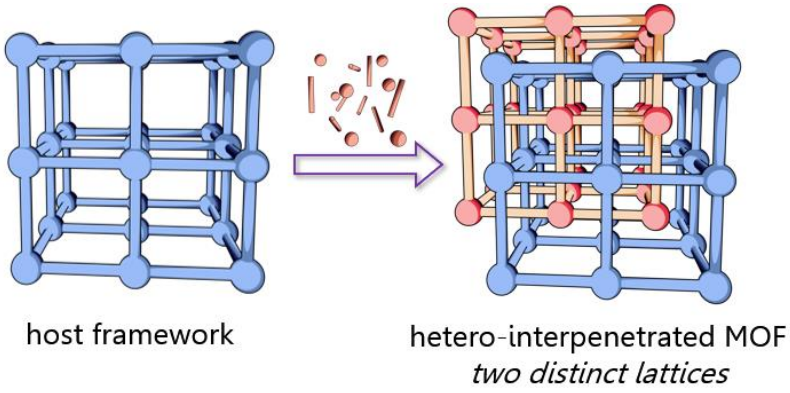

Interpenetrated metal-organic frameworks (MOFs) comprise two or more lattices that are mutually entangled. Interpenetration tunes the structures and pore architectures of MOFs to influence their interactions with guest molecules. Typically, the interpenetrating sublattices are identical. Hetero-interpenetrated MOFs, in contrast, have sublattices that are different to one another. While they can be produced by serendipity, to develop a deliberate strategy for making hetero-interpenetrated MOFs we employed the cubic α-MUF-9 framework as a host sublattice. α-MUF-9 is able to template the secondary growth of a second, interpenetrating, sublattice in its pores to produce hetero-interpenetrated MOFs. In certain cases, the sublattices cannot be produced via standalone reactions and are observed here for the first time. Unique functional properties are enabled by hetero-interpenetrated MOFs such as asymmetric catalysis. We grew a catalytically-active sublattice inside α-MUF-10, a chiral host. The chiral pore environment of the host imparts asymmetry on the catalytic activity of interpenetrating sublattice to give reaction products with an enantiomeric excess. This deliberate strategy for synthesizing hetero-interpenetrated MOFs opens new perspectives on framework structures and pore environments and allows unprecedented functional properties to emerge.

Introduction

Interpenetration[1,2] is a common phenomenon in metal-organic frameworks (MOFs) where entangled, interlocked sublattices exist in the same crystal. Methods to control interpenetration are important since interpenetration governs the size and chemical environment of the pores, the diffusivity of guest molecules, and the framework stability.[3-8] A longstanding target in MOF chemistry has been the deliberate synthesis of frameworks with interpenetrating sublattices that are chemically distinct from each other. Such *hetero-interpenetrated* MOFs are fascinating from design and structural viewpoints, and they may exhibit properties that are not observed in the individual lattices in isolation. For example, bringing together donor groups on one network with acceptor groups on another may result in new optical, magnetic and/or electronic characteristics. Complementary functional groups may also be precisely placed in the pores of hetero-interpenetrated MOFs to deliver unique adsorption, catalysis and sensing applications. Although occasional examples of hetero-interpenetrated MOFs have been discovered serendipitously,[3,9-12] their deliberate synthesis remains elusive. Recent computational studies have identified sub-lattices that are mutually compatible *in silico*, however these putative hetero-interpenetrated MOFs have not been experimentally realised.[13,14] Under conventional synthetic protocols, one-pot methods using structurally-related ligands will typically produce multivariate frameworks,[15] while ligands with different geometries either produce multicomponent MOFs[16] or mixed phases in preference to hetero-interpenetrated MOFs.

To address this challenge, we formulated a two-step methodology for the deliberate synthesis of hetero-interpenetrated MOFs. Initially, we grow a non-interpenetrated MOF that acts as a host sublattice. In a subsequent step, a second, interpenetrating framework is grown in the pore space of the first by secondary growth (Figure 1c). While the second sublattice must be geometrically compatible with the host, it can be chemically distinct so that secondary growth delivers a hetero-interpenetrated framework. There is potential for this strategy to be disrupted by competing processes. For example, the second framework may grow outside the pores of the first in a separate phase, the

47 incoming components may displace those of the original framework, or the second framework may be
48 hindered by mass transfer requirements. We herein present the successful realisation of this strategy
49 that circumvents these potential limitations.

50 Our strategy starts from α-MUF-9 (MUF = Massey University Framework), which is a cubic
51 MOF with a **pcu** lattice built up from Zn_4O nodes and linear dicarboxylate linkers (**L1**, Figure 1).[17]
52 Non-interpenetrated MUF-9 (denoted as α-MUF-9) can be synthesized in a bulky solvent such as DBF
53 (*N*,*N*-di-*n*-butylformamide). In earlier work, we found that α-MUF-9 promoted the growth of a second
54 [Zn_4O(**L1**)$_3$] lattice via favourable noncovalent interactions to produce β-MUF-9, a conventional
55 homo-interpenetrated MOF (Figure 1b). We speculated that secondary growth could instead take place
56 using sublattices with different compositions but the same metric parameters (Figure 1c). This was
57 achieved using zinc(II) or cobalt(II) metal ions to build up the M_4O clusters and ligands based on
58 biphenyl-4,4'-dicarboxylate and its close analogues.

59 The concept of *partial interpenetration* is central to this work. In most interpenetrated MOFs the
60 number of interpenetrating lattices is an integer. However, in partially interpenetrated MOFs different
61 regions of the crystal comprise different numbers of sublattices.[17-20] This results in a fractional value
62 for the overall level of partial interpenetration (PIP%). For a doubly interpenetrated MOF the PIP%
63 corresponds to the occupancy of the second sublattice. In some reported cases the PIP% is fixed[18,19]
64 while in others it can be controlled.[17,20]

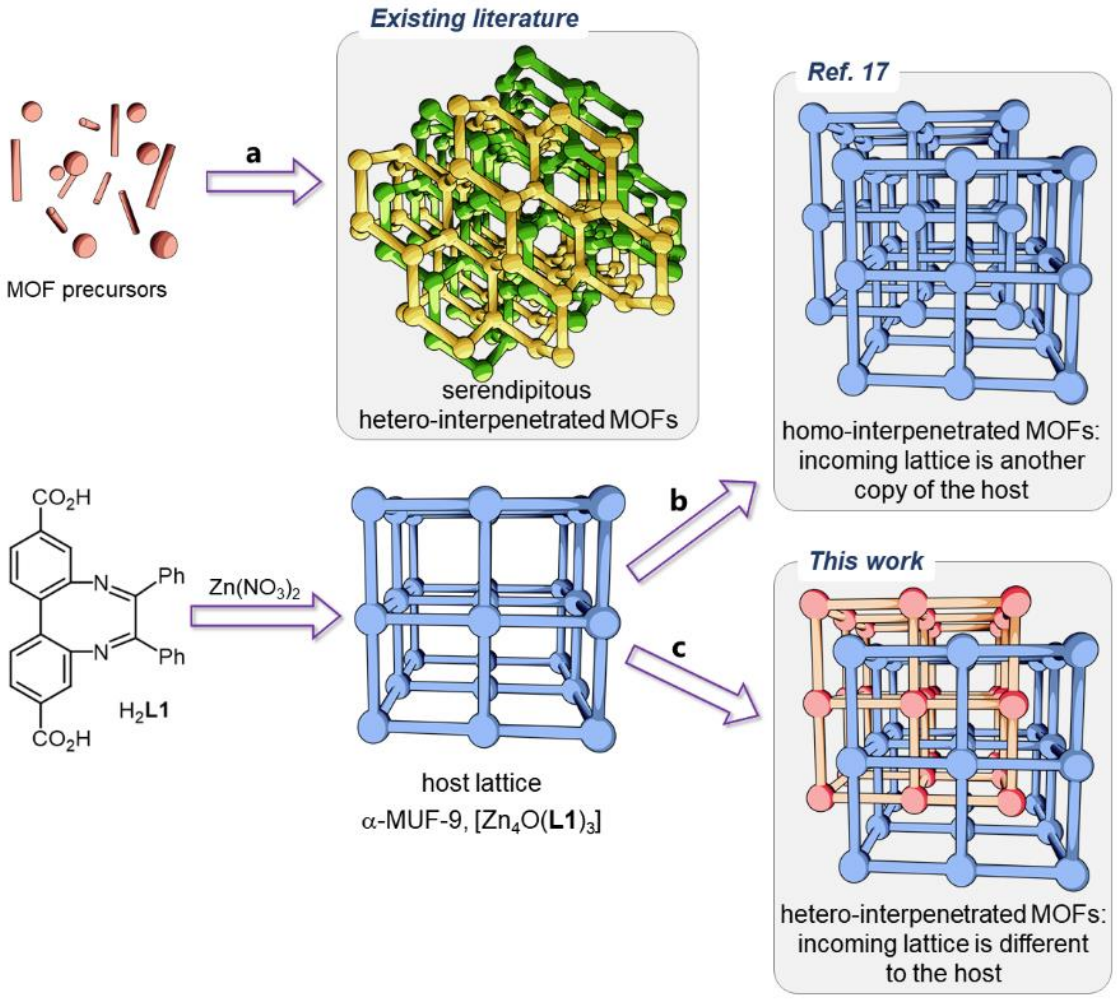

Figure 1: Hetero- and homo-interpenetrated MOFs. a) Occasional examples of the serendipitous formation of hetero-interpenetrated MOFs have been reported. b) Non-interpenetrated α-MUF-9 can serve as a host for the growth of another copy of the $[Zn_4O(\mathbf{L1})_3]$ lattice to make conventional, homo-interpenetrated MOFs. c) A design strategy for hetero-interpenetrated MOFs where α-MUF-9 templates a second sublattice that is chemically distinct from $[Zn_4O(\mathbf{L1})_3]$.

Results and discussion

MUF-91. Our first target was MUF-91 in which a $[Zn_4O(bpdc)_3]$ sublattice interpenetrates α-MUF-9 ($[Zn_4O(\mathbf{L1})_3]$, Figure 2a). We first prepared α-MUF-9 then incubated it in a secondary growth solution comprising 4,4'-biphenyldicarboxylic acid (H_2bpdc) and $Zn(NO_3)_2$ in DBF. We found 2-fluorobenzoic acid (FBA) to be a useful additive to suppress the formation of a standalone phase of $[Zn_4O(bpdc)_3]$. The PIP% of MUF-91, which equates to the occupancy of the interpenetrating $[Zn_4O(bpdc)_3]$ sublattice, increases over time and can be determined quantitatively by SCXRD, PXRD

and ^{1}H NMR spectroscopy (Figure 2d). A crystallographic model was developed for the SCXRD datasets (Figure 3b, Tables S1 and S2). The occupancy of the secondary [$Zn_4O(bpdc)_3$] sublattice was refined as a free variable to give a direct measure of the PIP% over the course of secondary growth. Restraints were used to ensure refinement stability and chemical correctness, and these were loosened as far as the data quality would allow. The *P*-43*m* space group of α-MUF-9 is consistently maintained. After nine hours, the PIP% reaches a value of 70%, which is the upper limit for the occupancy of the [$Zn_4O(bpdc)_3$] sublattice (Figure 2d). We could also gauge the PIP% over time by quantifying the changes in the PXRD patterns, and excellent agreement with the SCXRD data was observed. The intensity of the PXRD peak at $2\theta = 5.2°$ decreases in intensity and the peak at 7.3° increases (Figure S1). These correspond to the (100) and (110) reflections that are, respectively, extinguished and enhanced by the growing [$Zn_4O(bpdc)_3$] sublattice. These changes mirror those observed during the homo-interpenetration of MUF-9.[17] In accord with the diffraction data, ^{1}H NMR spectroscopic analysis of digested MUF-91 samples show that the amount of bpdc relative to **L1** increases with time. The PIP% deduced from the bpdc:**L1** ratio measured by ^{1}H NMR spectroscopy matches the PIP% given by the diffraction data for the first nine hours of secondary growth (Figure 2d). This confirms that bpdc does not simply displace **L1** from the [$Zn_4O(\mathbf{L1})_3$] host sublattice. After nine hours, the MUF-91 crystals begin to form a shell of a different phase, which is clearly distinguishable by optical microscopy (Figure S3). After this point, the bpdc:**L1** ratio measured by ^{1}H NMR spectroscopy increases beyond the PIP%, indicating that the shell comprises bpdc and has no **L1**. To optimise the occupancy of the interpenetrating lattice, we prepared MUF-91 starting from *microcrystalline* α-MUF-9 rather than large single crystals (Figure S6). PIP% values of ~75% were obtained since the smaller particle size allows for more rapid mass transport during secondary growth. As a control experiment, α-MUF-9 was incubated with H_2bpdc and FBA in DBF. Over a period of nine hours, only 4% of the **L1** linkers in MUF-9 were displaced by bpdc (Figure S28), which places an upper bound on the exchange that can occur during the synthesis of MUF-91. The well-controlled formation of hetero-

interpenetrated MUF-91 via secondary growth contrasts with the direct reaction of H_2**L1**, H_2bpdc, and $Zn(NO_3)_2$ in DEF. This reaction produces a cubic, doubly interpenetrated framework with the **L1** and bpdc linkers distributed randomly throughout the two sublattices i.e., a multivariate, homo-interpenetrated framework.

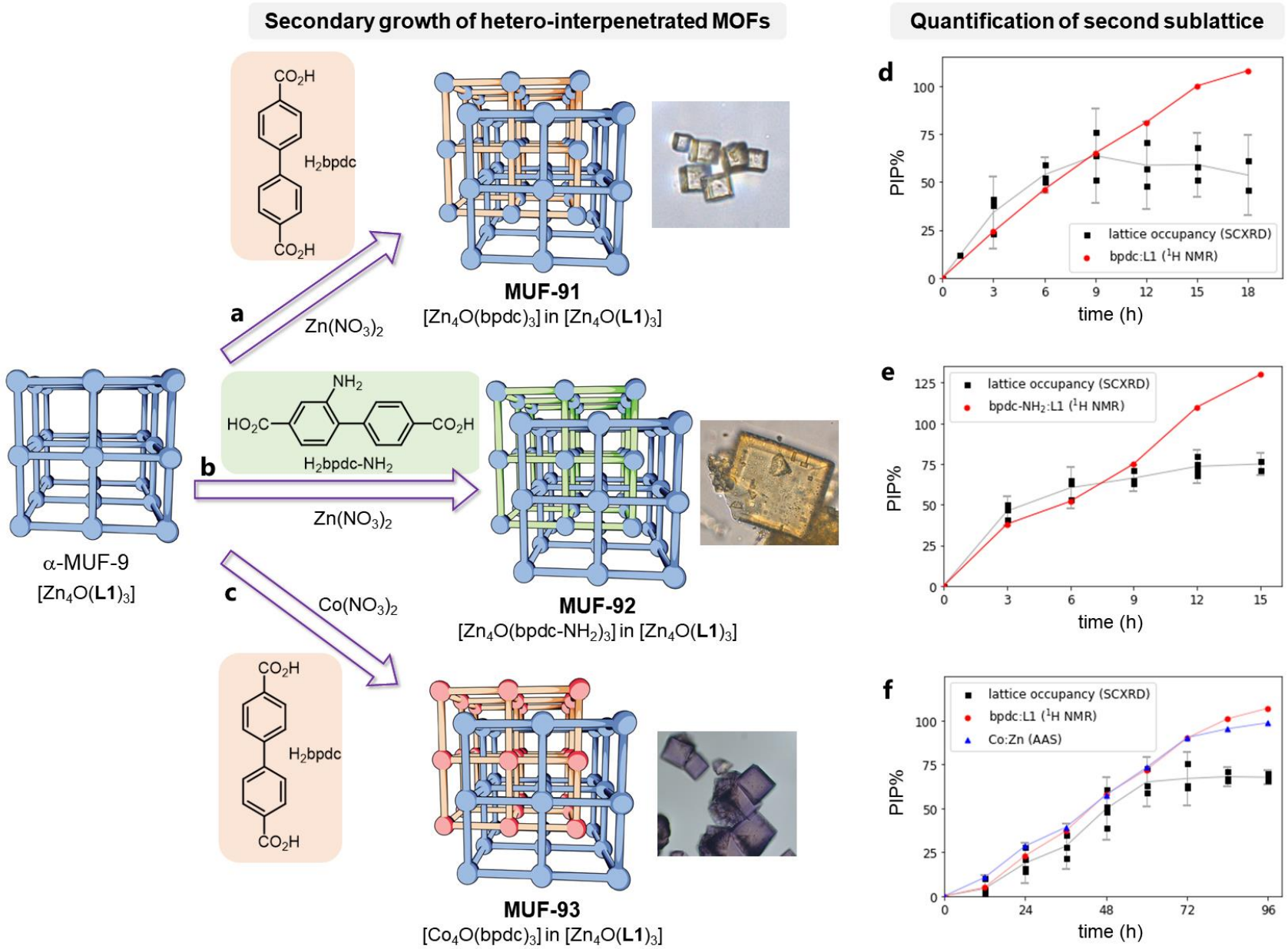
Secondary growth of hetero-interpenetrated MOFs
Quantification of second sublattice
α-MUF-9
[Zn4O(L1)3]
a
Zn(NO3)2
H2bpdc
MUF-91
[Zn4O(bpdc)3] in [Zn4O(L1)3]
b
Zn(NO3)2
H2bpdc-NH2
MUF-92
[Zn4O(bpdc-NH2)3] in [Zn4O(L1)3]
c
Co(NO3)2
H2bpdc
MUF-93
[Co4O(bpdc)3] in [Zn4O(L1)3]
d
PIP%
time (h)
lattice occupancy (SCXRD)
bpdc:L1 (1H NMR)
e
PIP%
time (h)
lattice occupancy (SCXRD)
bpdc-NH2:L1 (1H NMR)
f
PIP%
time (h)
lattice occupancy (SCXRD)
bpdc:L1 (1H NMR)
Co:Zn (AAS)

Figure 2: The experimental strategy towards hetero-interpenetrated MOFs, MUF-91, MUF-92 and MUF-93. α-MUF-9 (non-interpenetrated [Zn_4O(**L1**)$_3$]) is used as a host sublattice for the growth of the interpenetrating sublattices. (a) The synthesis of MUF-91 ([Zn_4O(bpdc)$_3$] in [Zn_4O(**L1**)$_3$]). (b) The synthesis of MUF-92 ([Zn_4O(bpdc-NH_2)$_3$] in [Zn_4O(**L1**)$_3$]). (c) The synthesis of MUF-93 ([Co_4O(bpdc)$_3$] in [Zn_4O(**L1**)$_3$]). The partial interpenetration level (PIP%) as a function of time as deduced from various experimental techniques for (d) MUF-91, (e) MUF-92, and (f) MUF-93. Black squares represent the fractional interpenetration of individual crystals as determined from SCXRD datasets. Red circles represent the ratio of **L1** to the ligand of the interpenetrating sublattice as determined by ^{1}H NMR spectroscopy. Blue triangles represent the ratio of zinc(II) to cobalt(II) in MUF-93 as determined by atomic absorption spectroscopy.

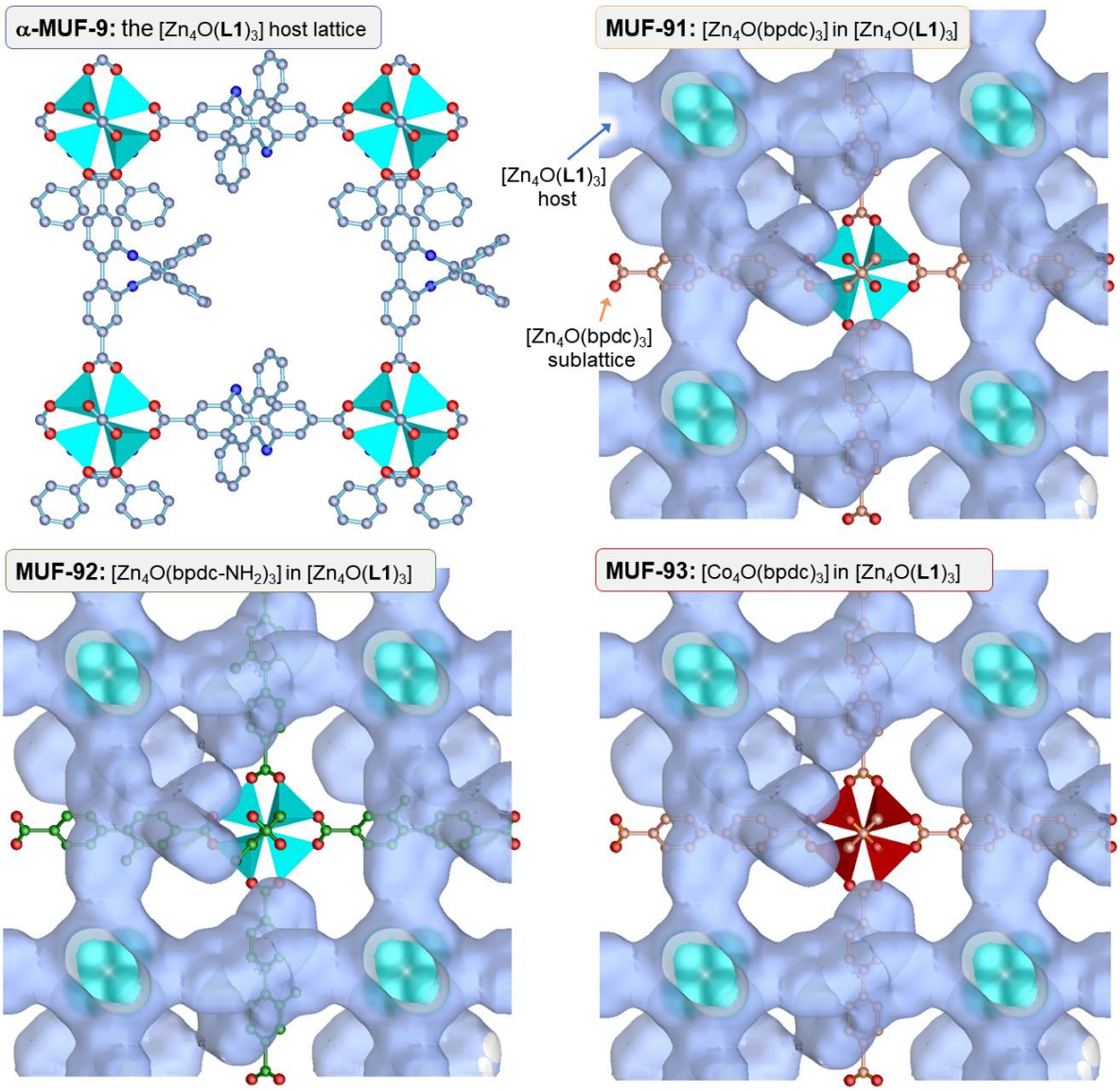

Figure 3: The structures of α-MUF-9 and MUF-91 – MUF-93, as determined by SCXRD. The interpenetrating sublattices, $[Zn_4O(bpdc)_3]$, $[Zn_4O(bpdc\text{-}NH_2)_3]$, and $[Co_4O(bpdc)_3]$ in MUF-91, MUF-92 and MUF-93, respectively, are shown with a ball-and-stick model and the van der Waals surface of α-MUF-9 is shown in blue. Hydrogen atoms are omitted for clarity and representative positions of the symmetry-disordered **L1** ligands are shown.

MUF-92. MUF-92 comprises [Zn_4O(bpdc-NH_2)$_3$] (bpdc-NH_2 = 2-amino-4,4'-biphenyldicarboxylate) interpenetrated in α-MUF-9 (Figure 2b). [Zn_4O(bpdc-NH_2)$_3$] is not known to form as a standalone framework,[21] but it is observed here courtesy of the templating effect of the [Zn_4O(**L1**)$_3$] host sublattice. The secondary growth conditions for MUF-92 used α-MUF-9 crystals together with H_2bpdc-NH_2, $Zn(NO_3)_2$, and FBA in DBF. We monitored the growth of the [Zn_4O(bpdc-NH_2)$_3$] sublattice by SCXRD, PXRD, and ^{1}(Figures 2e, S7 and S8, Table S3). The [Zn_4O(bpdc-NH_2)$_3$] sublattice grows in over an incubation period of nine hours to reach a PIP level of 74%. The phenyl rings of the bpdc-NH_2 ligand adopt an orthogonal conformation, which is impossible for **L1** and thus allows the two sublattices in MUF-92 to be unambiguously differentiated by SCXRD (Figure 3c). This indicates there is little, if any, displacement of the linkers from the [Zn_4O(**L1**)$_3$] sublattice by bpdc-NH_2, which was additionally verified by a control experiment (Figure S30). Beyond nine hours, a shell layer comprising bpdc-NH_2 and Zn(II) grows around the crystals (Figure S9), which means the **L1**:bpdc-NH_2 ratio deduced by NMR spectroscopy continues to rise while the PIP level of the MUF-92 core remains constant. When microcrystals of α-MUF-9 are used for secondary growth, the occupancy level of the [Zn_4O(bpdc-NH_2)$_3$] sublattice in MUF-92 reaches ~73% before it is inhibited by the Zn(II)/bpdc-NH_2 shell layer (Figures S11 and S12).

MUF-93. MUF-93 features α-MUF-9 interpenetrated by [Co_4O(bpdc)$_3$] (Figure 2c). [Co_4O(bpdc)$_3$] is not known as a standalone framework,[22] although a cobalt(II) analogue of MOF-5 has been reported starting from a preformed Co_4OL_6 cluster.[23] In MUF-93, the [Zn_4O(**L1**)$_3$] sublattice templates the formation of [Co_4O(bpdc)$_3$] under secondary growth conditions. The emergence of the [Co_4O(bpdc)$_3$] sublattice is evidenced by the purple coloration of the crystals together with SCXRD (Figure 3d), ^{1}H NMR spectroscopy and atomic adsorption (AA) spectroscopy . As deduced by XRD, large crystals of MUF-93 reach PIP levels of 70% over 60 hours of secondary growth (Figure 2f, Table S4), while starting from microcrystalline α-MUF-9 allows the [Co_4O(bpdc)$_3$] framework to reach 80% occupancy over just 18 hours (Figure S16). These PIP values align with the ^{1} indicates that there is

137 little displacement of the zinc(II) ions by cobalt(II). This is corroborated by the site-specific anomalous
138 scattering experiments detailed later. While the exchange of three out of four zinc(II) ions per node is
139 possible by heating α-MUF-9 in highly concentrated solutions of cobalt(II) nitrate in DBF (ESI,
140 Section S5.2), low rates of metal exchange during the secondary growth of MUF-93 were ensured by
141 using a low concentration of cobalt(II) nitrate. Once the$[Co_4O(bpdc)_3]$ sublattice reaches ~70%
142 the$[Zn_4O(\mathbf{L1})_3]$ by cobalt(II) and bpdc, respectively (Figure 2f).

143 The variation of PIP% within an individual specimen of MUF-93 was probed by systematically
144 collecting SCXRD datasets across the midpoint of a single crystal approximately ~180 μm in size
145 (Figure 4, Figure S13). Synchrotron X-ray radiation was used with a beam (spot size) on the crystal of
146 approximately 10 μm (FWHM) horizontally, and the crystal was 'rastered' to yield datasets from
147 various spatial regions. As anticipated, we observed the highest PIP% values (~72%) near both edges
148 of the crystal. The PIP levels drop to ~20% when the beam is directed at the centre of the crystal since
149 the PIP level is lower at the core.

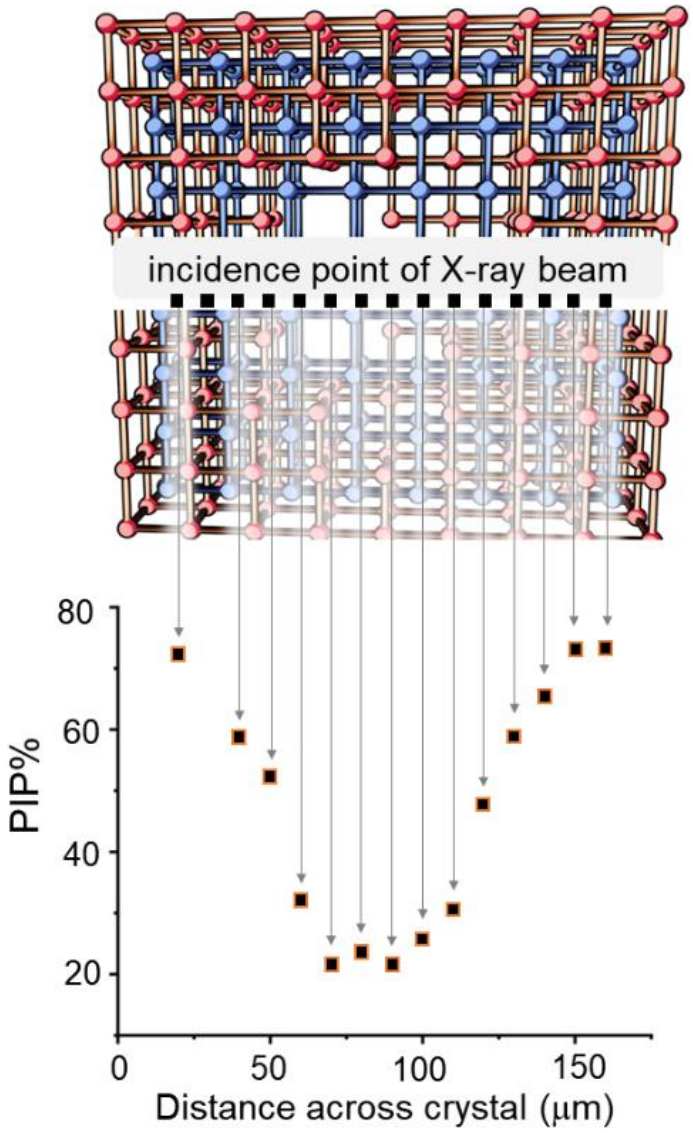

Figure 4: The variation in partial interpenetration across an individual crystal of MUF-93 as determined from multiple single-crystal synchrotron X-ray diffraction datasets. An illustration of a crystal of MUF-93 is presented showing the region 'rastered' by the synchrotron X-ray beam. The occupancy level of the interpenetrating $[Co_4O(bpdc)_3]$ sublattice is highest towards the edges of the crystal and lowest at its centre. Obviously, the number of unit cells actually present in the X-ray beam at each data collection point is many orders of magnitude greater than that illustrated.

Conventional single-crystal diffraction cannot reliably distinguish cobalt from zinc in MUF-93 because of their similar electron counts. This is exacerbated at low PIP levels due to high correlations between scattering factors, occupancy and atomic displacement parameters. However, tuning the X-ray wavelength to be near the respective absorption edges for cobalt and zinc enhances their anomalous

dispersion and, in principle, permits the discrimination and quantification of these metals at specific crystallographic sites (Figure S18).[24-26] On this basis, we developed a new method for using anomalous dispersion to differentiate metals in crystalline materials. For MUF-93, we calculated the differences in reflection intensities between datasets collected just below the cobalt(II) absorption edge at 7500 eV (where the in-phase (*f*') anomalous scattering contribution by cobalt is significant) and a high-resolution dataset collected at 17440 eV (where there is little anomalous scattering) on the same crystal. The reflection intensity differences obtained in this way arise partly from the difference in anomalous scattering by the cobalt and thus can be used to locate and quantify the cobalt sites. Similarly, we used 9670/17440 eV difference datasets, which maximize zinc anomalous dispersion, to pinpoint the zinc sites. Figure 5 illustrates the datasets obtained in this way, showing differences between peaks near the unit cell centre (crystallographically identical metal atom sites of the $[Zn_4O(\mathbf{L1})_3]$ host sublattice) and peaks near the unit cell corners (crystallographically identical metal atom sites of the interpenetrating $[Co_4O(bpdc)_3]$ sublattice). After a secondary growth time of 60 hours the occupancy of $[Co_4O(bpdc)_3]$ in MUF-93 reaches its maximum. At this point, a distinct peak for cobalt appears near the corner of the unit cell in the difference datasets due to the cobalt ion in the $[Co_4O(bpdc)_3]$ sublattice (Figure 5a). No signal for cobalt can be detected near the midpoint of the unit cell, which demonstrates that cobalt(II) ions do not displace zinc(II) ions from the $[Zn_4O(\mathbf{1})_3]$ host over the 60 hours of secondary growth. Displacement of the zinc(II) ions in the $[Zn_4O(\mathbf{L1})_3]$ sublattice only becomes evident after a much longer reaction time (Figure 5b).

Two illustrative control experiments were also performed. First, a 7500/17440 eV difference dataset on a crystal of α-MUF-9 in which the zinc(II) ions had been partially replaced by cobalt(II) showed a single peak for cobalt near the midpoint of the unit cell and no sign of an interpenetrating lattice (Figure S19c). Second, a 9670/17440 eV difference dataset for homo-interpenetrated β-MUF-9 revealed two equally strong peaks for the two independent zinc sites in the unit cell (in the *P*-43*m* space group), as expected (Figure S19d).

The anomalous dispersion experiments clearly show that the two sublattices in MUF-93 are distinct from each other and thus the framework can be genuinely described as being hetero-interpenetrated. This observation underscores power of the two-step strategy involving secondary growth (Figure 1) since any attempt to directly synthesize MUF-93 starting from a mixture of H_2bpdc, $Zn(NO_3)_2$, and $Co(NO_3)_2$ would result in a mixed-metal multivariate material.

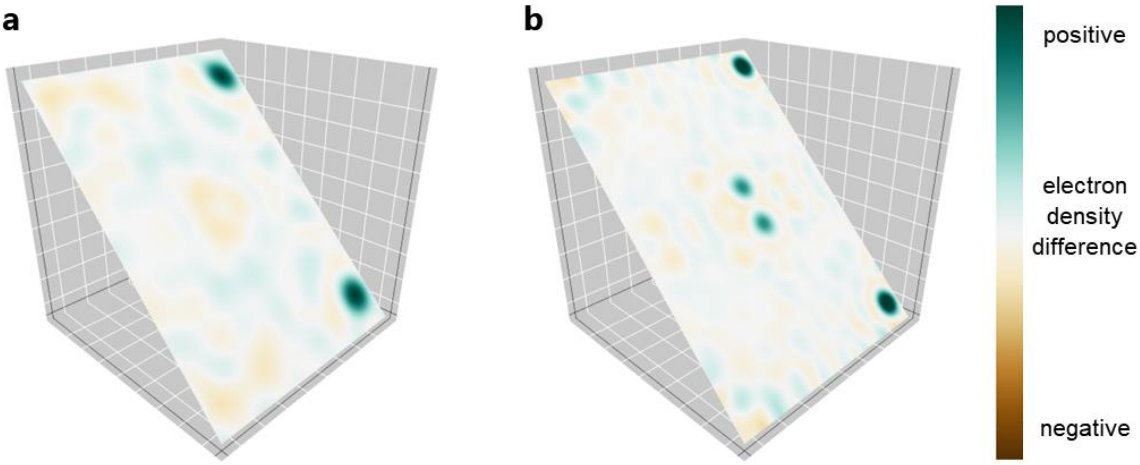

Figure 5: Slices of the (1,0,1) plane of the (F_{obs}, Φ_{calc}) electron density difference maps from datasets collected at 17440 eV and 7500 eV. The colour scale indicates the difference electron density as green (positive) or brown (negative). Peaks near the corner of the unit correspond to cobalt occupying the M_4O cluster sites of the interpenetrating sublattice, and peaks near the midpoint of the unit cell to cobalt occupying the cluster sites of the host sublattice. (a) MUF-93 after 60 hours of secondary growth showing cobalt(II) occupying the M_4O cluster sites in the interpenetrating $[Co_4O(bpdc)_3]$ sublattice; a negligible quantity of it displaces zinc(II) from the $[Zn_4O(\mathbf{L1})_3]$ host sublattice. (b) MUF-93 after 168 hours of secondary growth showing that after this prolonged reaction time a significant amount of cobalt(II) occupies the M_4O cluster sites of both sublattices. In this case it has displaced some zinc(II) ions from the host $[Zn_4O(\mathbf{L1})_3]$ sublattice.

(R)-MUF-101 and (S)-MUF-101 as catalysts. Hetero-interpenetrating frameworks constitute a design blueprint for unique functional properties. To illustrate this, we installed the two key roles of an asymmetric catalyst – catalytically activity and chirality – onto the two *different* sublattices of a hetero-interpenetrated MOF. α-MUF-10 is a noninterpenetrated, chiral MOF comprising (R)- or (S)-**L1** (Figure 6). α-MUF-10 act as the host sublattice and its pore spaces in provide a chiral environment for asymmetric catalysis. An achiral interpenetrating [Zn_4O(**L2**)$_3$] sublattice delivers the catalytic activity. We selected **L2** to generate this sublattice since secondary amines are known to be effective organocatalysts for a range of reactions.[27,28] We found that α-(R)-MUF-10 or α-(S)-MUF-10 ([Zn_4O((R)-**L1**)$_3$] or [Zn_4O((S)-**L1**)$_3$]) templates the growth of [Zn_4O(**L2**)$_3$] to produce MUF-101 (Figure 6). We employed MUF-101 with PIP level of 15% as a catalyst to retain a large void volume and thus maximise mass transfer.

With a catalyst loading of 0.5% (defined as the molar ratio of catalytic **L2** units to aldehyde), MUF-101 catalyses the Henry reaction between 2-chloro-5-nitrobenzaldehyde (**1**) and nitromethane. HPLC revealed the chiral reaction product (**2**) to have an enantiomeric excess of −9.4% when catalyzed by (R)-MUF-101 (Table S7). To our delight, the enantioselectivity was reversed when (S)-MUF-101 was used as the catalyst. This confirms that the preferred handedness of the reaction product arises from the chirality of the MUF-10 host sublattice.

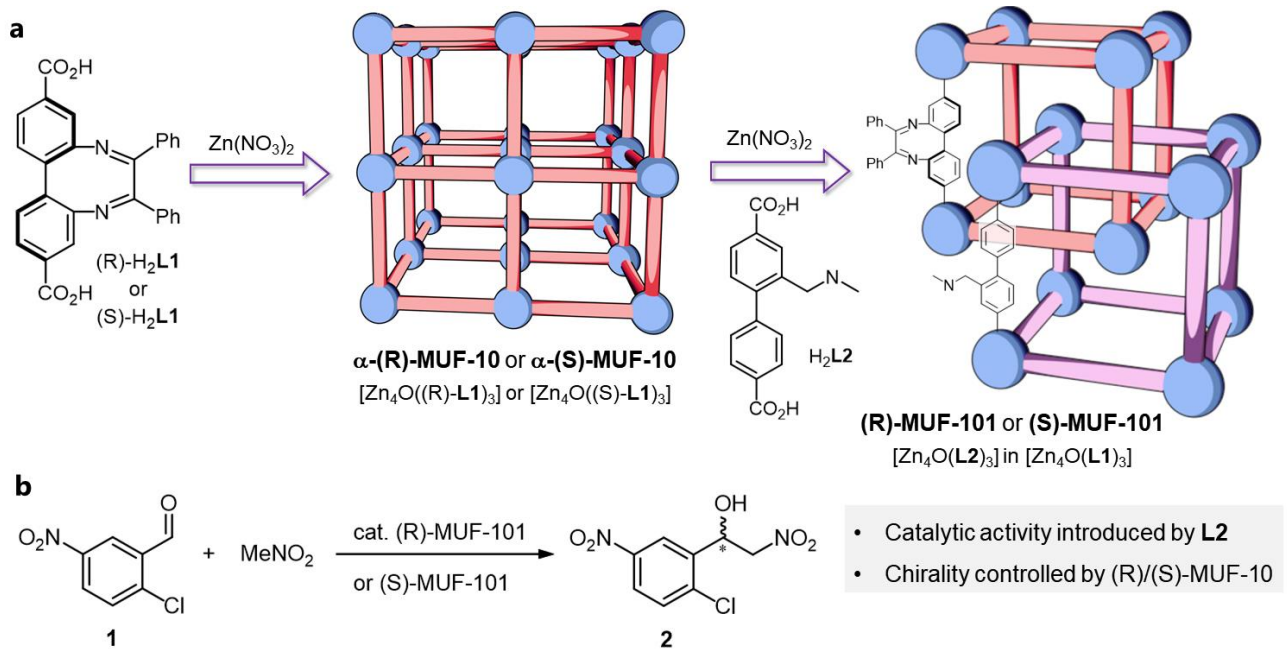

204

Figure 6: In MUF-101, chiral α-(R)-MUF-10 or α-(S)-MUF-10 hosts a catalytically-active, yet achiral, [Zn_4O(**L2**)$_3$] sublattice. MUF-101 acts as an asymmetric catalyst by coupling the chirality of the host to the catalytic activity of the interpenetrating sublattice. (a) The synthetic route to MUF-101. (b) The Henry reaction between 2-chloro-5-nitrobenzaldehyde and nitromethane is catalyzed by MUF-101 and produces **2** with an enantiomeric excess that changes sign depending on whether α-(R)-MUF-10 or α-(S)-MUF-10 is used as the host sublattice.

205

206 ## Outlook

207 The rational design of hetero-interpenetrated MOFs has inherent challenges since the component
208 sublattices must be geometrically and chemically compatible, phase separation is possible, and
209 exchange of the metal ions and linkers may occur. We have overcome these obstacles to develop a
210 synthetic approach that takes advantage of the templating effect of a host lattice to promote the growth
211 of interpenetrating sublattices in a second, discrete step. These hetero-interpenetrated MOFs retain the
212 make-up of the individual sublattices since there is no significant exchange of components between
213 them. In certain cases, the interpenetrating sublattices cannot be produced via standalone reactions and
214 are observed here for the first time.

This deliberate strategy to hetero-interpenetrated MOFs opens new perspectives on the field of framework chemistry Unique functional properties can emerge when *different* sublattices are coupled to one another. Here, we show how the two principal roles of an asymmetric catalyst can be assigned to the different sublattices: the host framework provides a chiral environment for the second, catalytically active, sublattice. The enantioselectivity is dictated by the handedness of the host sublattice in a way that is reminiscent of the active site in enzymes where the chirality of the catalytic pocket influences the reaction stereochemistry. Further functional properties that draw on other complementary attributes of interpenetrating sublattices are now within reach.

Acknowledgements

This research was undertaken in part using the MX2 beamline at the Australian Synchrotron, part of ANSTO. We made use of the Australian Cancer Research Foundation (ACRF) detector, part-funded by the New Zealand Group Ltd for which support from Massey University is gratefully acknowledged. We are grateful to beamline scientists Dr Santosh Panjikar and Dr Jason Price for their expert help. We also thank Mr David Lun and Dr Lauren Macreadie for technical assistance and Professor Paul Plieger for guidance on AA spectroscopy.

Author contributions

S.G.T. conceived of the presented idea. A.F. conducted preliminary experiments while D.P. developed the idea, conducted experiments, analyzed the results, and prepared the supplementary information. S.J.L. conducted experimental work. G.B.J. conceived and advised on the anomalous scattering experiments. S.G.T. and G.B.J. supervised the project. All authors contributed to the final manuscript.

References

1. Batten, S. R. Topology of Interpenetration. *CrystEngComm* **2001**, *3*, 67-72.

2. Batten, S. R.; Robson, R. Interpenetrating Nets: Ordered, Periodic Entanglement. *Angew. Chem., Int. Ed.* **1998**, *37*, 1460-1494

3. Haldar, R.; Sikdar, N.; Maji, T. K. Interpenetration in Coordination Polymers: Structural Diversities toward Porous Functional Materials. *Mater Today* **2015**, *18*, 97-116.

4. Jiang, H.-L.; Makal, T. A.; Zhou, H.-C. Interpenetration Control in Metal–Organic Frameworks for Functional Applications. *Coord. Chem. Rev.* **2013**, *257*, 2232-2249.

5. Park, J. H.; Lee, W. R.; Kim, Y.; Lee, H. J.; Ryu, D. W.; Phang, W. J.; Hong, C. S. Interpenetration Control, Sorption Behavior, and Framework Flexibility in Zn(Ii) Metal–Organic Frameworks. *Cryst. Growth Des.* **2014**, *14*, 699-704.

6. Verma, G.; Butikofer, S.; Kumar, S.; Ma, S. Regulation of the Degree of Interpenetration in Metal-Organic Frameworks. *Top. Curr. Chem.* **2019**, *378*, 4.

7. Deshpande, R. K.; Minnaar, J. L.; Telfer, S. G. Thermolabile Groups in Metal-Organic Frameworks: Suppression of Network Interpenetration, Post-Synthetic Cavity Expansion and Protection of Reactive Functional Groups. *Angew. Chem. Int. Ed.* **2010**, *47*, 4598-4602.

8. Miller, J. S. Interpenetrating Lattices—Materials of the Future. *Adv. Mater.* **2001**, *13*, 525-527.

9. Li, S.; Li, G.-L.; Wang, W.; Liu, Y.; Cao, Z.-M.; Cao, X.-l.; Huang, Y.-G. A 2d Metal-Organic Framework Interpenetrated by a 2d Supramolecular Framework Assembled by Ch/Π Interactions. *Inorg. Chem. Commun.* **2021**, *130*, 108705.

10. Zhang, M.-D.; Di, C.-M.; Qin, L.; Yang, Q.-X.; Li, Y.-Z.; Guo, Z.-J.; Zheng, H.-G. Chiral 3d/3d Hetero-Interpenetrating Framework with Six Kinds of Helices, 3d Polyrotaxane and 2d Network Via One-Pot Reaction. *CrystEngComm* **2013**, *15*, 227-230.

11. Xu, H.; Bao, W.; Xu, Y.; Liu, X.; Shen, X.; Zhu, D. An Unprecedented 3d/3d Hetero-Interpenetrated Mof Built from Two Different Nodes, Chemical Composition, and Topology of Networks. *CrystEngComm* **2012**, *14*, 5720-5722.

12. Batten, S. R.: Topology and Interpenetration. In *Metal-Organic Frameworks: Design and Application*; MacGillivray, L. R., Ed.; John Wiley & Sons, 2010.

13. Kwon, O.; Park, S.; Zhou, H. C.; Kim, J. Computational Prediction of Hetero-Interpenetration in Metal-Organic Frameworks. *Chem. Commun.* **2017**, *53*, 1953-1956.

14. Sezginel, K.; Feng, T.; Wilmer, C. Discovery of Hypothetical Hetero-Interpenetrated Mofs with Arbitrarily Dissimilar Topologies and Unit Cell Shapes. *CrystEngComm* **2017**, *19*, 4497-4504.

15. Furukawa, H.; Muller, U.; Yaghi, O. M. "Heterogeneity within Order" in Metal-Organic Frameworks. *Angew Chem Int Ed Engl* **2015**, *54*, 3417-3430.

16. Pang, Q.; Tu, B.; Li, Q. Metal–Organic Frameworks with Multicomponents in Order. *Coord. Chem. Rev.* **2019**, *388*, 107-125.

17. Ferguson, A.; Liu, L.; Tapperwijn, S. J.; Perl, D.; Coudert, F.-X.; Van Cleuvenbergen, S.; Verbiest, T.; van der Veen, M. A.; Telfer, S. G. Controlled Partial Interpenetration in Metal–Organic Frameworks. *Nat. Chem.* **2016**, *8*, 250-257.

18. Verma, G.; Kumar, S.; Pham, T.; Niu, Z.; Wojtas, L.; Perman, J. A.; Chen, Y.-S.; Ma, S. Partially Interpenetrated Nbo Topology Metal–Organic Framework Exhibiting Selective Gas Adsorption. *Cryst. Growth Des.* **2017**, *17*, 2711-2717.

19. Yang, S.; Lin, X.; Lewis, W.; Suyetin, M.; Bichoutskaia, E.; Parker, J. E.; Tang, C. C.; Allan, D. R.; Rizkallah, P. J.; Hubberstey, P.; et al. A Partially Interpenetrated Metal–Organic Framework for Selective Hysteretic Sorption of Carbon Dioxide. *Nat. Mater.* **2012**, *11*, 710–716.

20. O'Nolan, D.; Madden, D. G.; Kumar, A.; Chen, K. J.; Pham, T.; Forrest, K. A.; Patyk-Kazmierczak, E.; Yang, Q. Y.; Murray, C. A.; Tang, C. C.; Space, B.; Zaworotko, M. J. Impact of Partial Interpenetration in a Hybrid Ultramicroporous Material on C_2h_2/C_2h_4 Separation Performance. *Chem. Commun.* **2018**, *54*, 3488-3491.

21. Deshpande, R. K.; Minnaar, J. L.; Telfer, S. G. Thermolabile Groups in Metal-Organic Frameworks: Suppression of Network Interpenetration, Post-Synthetic Cavity Expansion, and Protection of Reactive Functional Groups. *Angew. Chem. Int. Ed.* **2010**, *49*, 4598-4602.

22. Pan, L.; Ching, N.; Huang, X.; Li, J. Reactions and Reactivity of Co− Bpdc Coordination Polymers (Bpdc= 4, 4 '-Biphenyldicarboxylate). *Inorg. Chem.* **2000**, *39*, 5333-5340.

23. Hausdorf, S.; Baitalow, F.; Böhle, T.; Rafaja, D.; Mertens, F. O. Main-Group and Transition-Element Irmof Homologues. *J. Am. Chem. Soc.* **2010**, *132*, 10978-10981.

24. Brozek, C. K.; Cozzolino, A. F.; Teat, S. J.; Chen, Y.-S.; Dincă, M. Quantification of Site-Specific Cation Exchange in Metal–Organic Frameworks Using Multi-Wavelength Anomalous X-Ray Dispersion. *Chem. Mater.* **2013**, *25*, 2998–3002.

25. Freedman, D. E.; Han, T. H.; Prodi, A.; Müller, P.; Huang, Q.-Z.; Chen, Y.-S.; Webb, S. M.; Lee, Y. S.; McQueen, T. M.; Nocera, D. G. Site Specific X-Ray Anomalous Dispersion of the Geometrically Frustrated Kagome Magnet, Herbertsmithite, $Zncu_3(Oh)_6cl_2$. *J. Am. Chem. Soc.* **2010**, *132*, 16185–16190.

26. Helliwell, M.; Helliwell, J.; Kaucic, V.; Zabukovec Logar, N.; Teat, S.; Warren, J.; Dodson, E. Determination of Zinc Incorporation in the Zn-Substituted Gallophosphate Znulm-5 by Multiple Wavelength Anomalous Dispersion Techniques. *Acta Cryst. B* **2010**, *66*, 345-357.

27. Zhou, T.-Y.; Auer, B.; Lee, S. J.; Telfer, S. G. Catalysts Confined in Programmed Framework Pores Enable New Transformations and Tune Reaction Efficiency and Selectivity. *J. Am. Chem. Soc.* **2019**, *141*, 1577-1582.

306 28. Ishikawa, H.; Shiomi, S. Alkaloid Synthesis Using Chiral Secondary Amine Organocatalysts. *Org.*
307 *Biomol. Chem.* **2016**, *14*, 409-424.
308

Supplementary Files

This is a list of supplementary files associated with this preprint. Click to download.

- MUF913h41pccheckcif.pdf
- MUF9115h51pccheckcif.pdf
- MUF9115h58pccifreport.pdf
- MUF9112h71pccifreport.pdf
- MUF9112h57pccheckcif.pdf
- MUF9115h68pccifreport.pdf
- MUF913h23pccifreport.pdf
- MUF9312h4pccheckcif.pdf
- MUF913h38pccifreport.pdf
- MUF911h12pccifreport.pdf
- MUF9118h46pccheckcif.pdf
- MUF9336h28pccheckcif.pdf
- MUF919h64pccifreport.pdf
- MUF923h50pccifreport.pdf
- MUF923h48pccifreport.pdf
- MUF929h63pccheckcif.pdf
- MUF913h27pccifreport.pdf
- MUF926h53pccheckcif.pdf
- MUF919h51pccifreport.pdf
- MUF93scan1pos1031pccheckcif.pdf
- MUF9324h15pccheckcif.pdf
- MUF916h52pccifreport.pdf
- MUF9312h10pccheckcif.pdf
- MUF9312h02pccheckcif.pdf
- MUF929h71pccheckcif.pdf
- MUF9372h63pccheckcif.pdf
- MUF93scan1pos823pccheckcif.pdf
- MUF9212h68pccheckcif.pdf
- MUF93scan1pos1573pccheckcif.pdf
- MUF9215h77pc2checkcif.pdf
- MUF9360h59pccheckcif.pdf

- MUF9384h71pc.pdf
- MUF93scan1pos1147pccheckcif.pdf
- MUF9348h61pccheckcif.pdf
- MUF9396h66pccheckcif.pdf
- MUF9396h70pccheckcif.pdf
- MUF9215h77pccheckcif.pdf
- MUF93scan1pos452pccheckcif.pdf
- MUF9324h28pccheckcif.pdf
- ms54ESIV12.pdf
- MUF9348h48pccheckcif.pdf
- MUF9212h71pccheckcif.pdf
- MUF916h50pccifreport.pdf
- MUF9360h73pccheckcif.pdf
- MUF9384h66pccheckcif.pdf
- MUF93scan1pos1365pccheckcif.pdf
- MUF93scan1pos623pccheckcif.pdf
- MUF9324h16pccheckcif.pdf
- MUF923h42pccifreport.pdf
- MUF919h76pccifreport.pdf
- MUF93scan1pos359pccheckcif.pdf
- MUF926h65pccheckcif.pdf
- MUF93scan1pos1473pccheckcif.pdf
- MUF9384h67pccheckcif.pdf
- MUF9372h62pccheckcif.pdf
- MUF9372h76pccheckcif.pdf
- MUF9360h63pccheckcif.pdf
- MUF93scan1pos721pccheckcif.pdf
- MUF93scan1pos1259pccheckcif.pdf
- MUF9212h81pccheckcif.pdf
- MUF926h63pccheckcif.pdf
- MUF9348h39pccheckcif.pdf
- MUF9324h14pccheckcif.pdf
- MUF9396h67pc.pdf
- MUF93scan1pos531pccheckcif.pdf

- MUF9348h51pccheckcif.pdf
- MUF93scan1pos926pccheckcif.pdf
- MUF93scan1pos172pccheckcif.pdf
- MUF9215h71pccheckcif.pdf
- MUF9336h22pccheckcif.pdf
- MUF9312h01pccheckcif.pdf
- MUF9324h21pccheckcif.pdf